Hydrodynamic parameters of a sandy soil determined by ground-penetrating radar inside a single ring infiltrometer

Emmanuel Léger, Albane Saintenoy, Yves Coquet

RESEARCH ARTICLE

Key Points:
- Monitoring the wetting front with on-ground GPR
- Obtaining the whole set of Mualem-van Genuchten parameters

Correspondence to:
E. Léger,
emmanuel.leger@u-psud.fr

Hydrodynamic parameters of a sandy soil determined by ground-penetrating radar inside a single ring infiltrometer

Emmanuel Léger[1,2], Albane Saintenoy[1,2], and Yves Coquet[3,4,5]

[1]Laboratoire GEOPS, UMR 8148, Université Paris Sud, Orsay, France, [2]CNRS, Orsay, France, [3]ISTO, UMR 7327, Université d'Orléans, Orléans, France, [4]CNRS/INSU, ISTO, UMR 7327, Orléans, France, [5]BRGM, ISTO, UMR 7327, Orléans, France

Abstract This study shows how Mualem-van Genuchten (M-vG) parameters can be obtained from GPR data acquired during water infiltration from a single ring infiltrometer in the case of a sandy soil. Water content profiles were generated at various time steps using HYDRUS-1D, based on particular values of the M-vG parameters and were converted to dielectric permittivity profiles using the Complex Refractive Index Method. The GprMax suite of programs was used to generate radargrams and to follow the wetting front progression in depth using the arrival time of the electromagnetic waves recorded by a ground-penetrating radar (GPR). Theoretically, the 1-D time convolution between reflectivity and GPR signal at any infiltration time step is related to the peak of the reflected signal recorded in the corresponding trace in the radargram. We used this relationship to invert the M-vG parameters for constant and falling head infiltrations using the Shuffled Complex Evolution (SCE-UA) algorithm. The method is presented on synthetic examples and on experiments carried out for a sandy soil. The parameters inverted are compared with values obtained in laboratory on soil samples and with disk infiltrometer measurements.

1. Introduction

Soil hydraulic properties, represented by the soil water retention $\theta(h)$ and hydraulic conductivity $K(h)$ functions, dictate water flow in the vadose zone, as well as partitioning between infiltration and runoff. Their evaluation has important implications for modeling available water resources and for flood forecasting, and is also crucial in evaluating the dynamics of chemical pollutants in soil and in assessing the risks of groundwater pollution.

Soil hydraulic functions can be described by several mathematical expressions [*Kosugi et al.*, 2002], among them the Mualem-van Genuchten (M-vG) function [*Mualem*, 1976; *van Genuchten*, 1980]. The determination of the parameters defining the van Genuchten soil water retention function is usually done using laboratory experiments, such as the water hanging column [*Dane and Hopmans*, 2002].

The hydraulic conductivity function can be estimated either in the laboratory, or in situ using infiltration tests. Among the large number of existing infiltration tests [*Angulo-Jaramillo et al.*, 2000], the single [*Muntz et al.*, 1905] or double ring infiltrometers [*Boivin et al.*, 1987] provide the field saturated hydraulic conductivity by applying a positive water tension to the soil surface, while the disk infiltrometer [*Perroux and White*, 1988; *Clothier and White*, 1981] allows reconstruction of the hydraulic conductivity curve $K(h)$ close to saturation, by applying different water pressures smaller than or equal to zero. For infiltration tests, the volume of infiltrated water versus time is fitted to infer the soil hydraulic conductivity. These tests are time consuming and their analysis involves various simplifying assumptions, partly due to the ignorance of the shape of the infiltration front. This lack of knowledge on the form of the infiltration bulb has to be fixed to get accurate information on the soil water retention $\theta(h)$ function and consequently on the hydraulic conductivity $K(h)$ function. This can be done by water content sensing.

Vereecken et al. [2008] and *Evett and Parkin* [2005] presented a state-of-the-art review on the different techniques available for soil moisture measurements. Among the large panel presented, geophysical methods take an important part, mainly because many of them are noninvasive and/or easy to use. Commonly used hydro-geophysical methods are electrical resistivity measurements [*Zhou et al.*, 2001; *Goyal et al.*, 2006] and electromagnetic methods [*Sheets and Hendrickx*, 1995; *Akbar et al.*, 2005]. This paper focuses on the use of ground-penetrating radar (GPR) as a tool for monitoring water infiltration in soil.

For a few decades, GPR has been known as an accurate method to measure water content variations in soils [*Huisman et al.*, 2003; *Annan*, 2005; *Doolittle et al.*, 2006]. Different techniques are available in the literature for monitoring water content in soils using GPR. Tomography imaging between boreholes during an infiltration has been used by *Binley et al.* [2001] and *Kowalsky et al.* [2005], among others [*Chen et al.*, 2001; *Endres et al.*, 2007]. Many advances were made in recent years with off-ground and cross-hole GPR using full-waveform inversion, for instance, to invert soil hydraulic properties [*Lambot et al.*, 2006, 2009; *Jadoon et al.*, 2012] and to identify high-porosity layers that act as zones of preferential flow [*Klotzsche et al.*, 2013]. *Grote et al.* [2002] and *Lunt et al.* [2005] used two-way travel time variations from a reflector at a known depth to monitor water content variation with time. Finally, multioffset GPR survey techniques, i.e., CMP (Common Mid Points) or WARR (Wide-Angle Reflection-Refraction), were carried out during infiltration by *Mangel et al.* [2012] and were used for water content estimation by *Greaves et al.* [1996] and *Bradford* [2006, 2008].

The work presented here is based on mono-offset monitoring of infiltration with on-ground surface GPR as discussed by *Haarder et al.* [2011], *Moysey* [2010], *Lai et al.* [2006, 2012], *Dagenbach et al.* [2013], and *Saintenoy et al.* [2008]. *Haarder et al.* [2011] used a constant offset on-ground GPR coupled with dye tracing to exhibit preferential flows. They found that GPR was able to map deep infiltration when compared to using dye tracer, but were unable to resolve the infiltration patterns (by-pass flow, fingering). *Moysey* [2010] studied the infiltration inside a sand box from the surface with on-ground GPR. He used the reflection from the wetting front as well as from the ground wave and the bottom of the box, to monitor change in water content. He also modeled his experiment and estimated the van Genuchten parameters using semblance analysis. He found that the most poorly constrained parameter was *n*, this parameter being linked to the curvature of the water retention curve [*Saintenoy and Hopmans*, 2011]. *Lai et al.* [2012] used a joint time frequency analysis coupled with gray scale imaging to measure infiltration and drainage under controlled laboratory conditions. They were able to follow the peak frequency of the GPR wavelet associated with the wetting front using time frequency analysis, from which the rate of water infiltration was determined. *Saintenoy et al.* [2008] monitored the wetting bulb during infiltration down an 81 cm long tube placed in the soil, and were able to identify the dimension of the bulb with time using GPR and good agreement was found between modeled and experimental radargrams.

Hydrological models contain many parameters that need to be fitted to fully describe hydrodynamic processes in porous media. This large multidimensionality of the parameter space complicates the process of finding the global minimum. This difficulty is mainly due to the existence of multiple local optima, to the discontinuity of the objective function and its first derivative, and to the nonlinear response of the models. These issues inspired many studies since the beginning of computing science, and browsing the literature about global optimization genesis is very instructive, particularly in hydrological science [*Vrugt et al.*, 2003, 2008]. Among the large panel of studies using direct search algorithms, many of them used the Nelder-Mead (Simplex) method [*Nelder and Mead*, 1965], proposed in the early 1960s and explained in detail by *Lagarias et al.* [1998]. As an illustrative instance, *Barati* [2011] used the Nelder-Mead algorithm to obtain the nonlinear Muskingum's model parameters to simulate rivers flooding. However, the Nelder-Mead method is described as "*not very efficient in terms of the number of function evaluations that it requires*" [*Press et al.*, 1988], and many studies on numerical analysis discredit the efficiency of this method [*Torczon*, 1989; *Wright*, 1996]. Many methods have been proposed to ameliorate this algorithm since its original version. For instance, one can denote the work of *Lambot et al.* [2002], who coupled the Nelder-Mead Simplex algorithm with the global multilevel coordinate search algorithm [*Huyer and Neumaier*, 1999] to invert soil hydraulic parameters.

One of the other ways to improve the Nelder-Mead algorithm consists in increasing the number of simplexes and make them evolve in parallel [*Torczon*, 1989], which is called multidimensional search method. These considerations inspired *Duan et al.* [1992] to develop a global optimization procedure, entitled the Shuffled Complex Evolution (SCE-UA) algorithm. Numerous studies have demonstrated that the SCE-UA algorithm is consistent, effective, and efficient in locating the optimal model parameters of a hydrological model. In particular, the recent studies of *Mboh et al.* [2011] and *Busch et al.* [2013] prove the efficiency of this algorithm to infer soil hydraulic parameters.

In the continuity of these studies, we present a method for monitoring the wetting front during infiltration using on-ground GPR with fixed offset inside a ring infiltrometer. The objectives of this paper are (i) to check if the proposed method is accurate enough to monitor the wetting front during infiltration in a sand soil

with different boundary conditions and (ii) to invert the M-vG parameters and the initial water content using the SCE-UA algorithm. We present synthetic examples and experimental field data sets.

2. Background

2.1. Unsaturated Flow Equation

In this study, we considered one-dimensional vertical soil water flow, described by the one-dimensional Richards' equation [*Richards*, 1931]. Its expression in terms of water content is:

$$\frac{\partial \theta}{\partial t} = \frac{\partial K(\theta)}{\partial z} + \frac{\partial}{\partial z}\left[D(\theta)\frac{\partial \theta}{\partial z}\right] \ , \tag{1}$$

where $K(\theta)$ is the hydraulic conductivity as a function of water content, and $D(\theta)$ is water diffusivity [*Childs and Collis-George*, 1950], expressed as $D(\theta) = K(\theta)\frac{\partial h}{\partial \theta}$, where h is pressure head.

2.2. Hydraulic Properties Functions

Several mathematical functions exist to model the hydraulic properties of porous media [*Kosugi et al.*, 2002]. We chose the *van Genuchten* [1980] model with the relation of *Mualem* [1976], with the following expression for the water retention curve:

$$\theta(h) = \theta_r + (\theta_s - \theta_r)(1 + (\alpha h)^n)^{\frac{1}{n}-1} \ , \tag{2}$$

where θ_s is the saturated water content, θ_r, the residual water content, and α and n define two fitting parameters which are, respectively, linked to the soil water matric potential and the slope of the water retention curve at the inflection point. The hydraulic conductivity function is described by:

$$K(\theta) = K_s \Theta^\lambda \left[1 - \left[1 - \Theta^{\frac{n}{n-1}}\right]^{\frac{n}{n-1}}\right]^2 \ , \tag{3}$$

with K_s the saturated hydraulic conductivity, $\Theta = \frac{\theta - \theta_r}{\theta_s - \theta_r}$ the effective saturation and λ accounts for pore tortuosity.

2.3. Petrophysical Relationships

Several empirical and conceptual relationships exist to convert volumetric water content to soil dielectric permittivity. Using the fact that the experiments presented here have been made in a quarry of Fontainebleau sand, considered as silica, we used the CRIM relation [*Birchak et al.*, 1974; *Roth et al.*, 1990], which relates the relative dielectric permittivity of bulk media, ε_b, to the volumetric summation of each components of it. Thus for a triphasic medium comprised of water, air, and silica, we obtain:

$$\sqrt{\varepsilon_b} = \theta\sqrt{\varepsilon_w} + (1-\phi)\sqrt{\varepsilon_s} + (\phi - \theta) \ , \tag{4}$$

where $\varepsilon_w = 80.1, \varepsilon_s = 2.5$ are, respectively, the relative dielectric permittivity of water and silica, ϕ the porosity, and θ the volumetric water content.

2.4. Dielectric Permittivity Versus Electromagnetic Wave Velocity

Surface GPR consists of a transmitting antenna, being a dipole, positioned on the surface, that emits short pulses of spherical electromagnetic (EM) waves in response to an excitation current source, and a receiving antenna, also located at the surface, which converts the incoming EM fields to an electrical signal source. Following the works of *Annan* [1999], the velocity of electromagnetic waves is:

$$v = \frac{c}{\sqrt{\varepsilon' \mu_r \frac{1+\sqrt{1+tan^2\delta}}{2}}} \ , \tag{5}$$

where δ is the loss factor as a function of the dielectric permittivity, frequency, and electrical conductivity, ε' denotes the real part of the relative dielectric permittivity, μ_r the relative magnetic permeability, and c

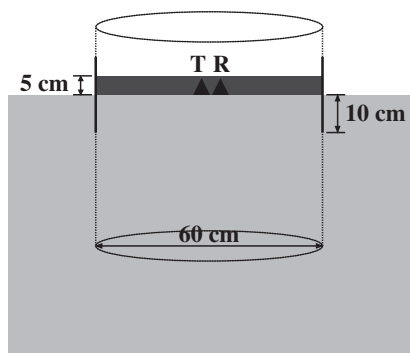LÉGER ET AL.   5461

Figure 1. Experimental setup at its initial state. T is the transmitter, R is the receiver. A 5 cm layer of water is set. The cylinder is buried in the soil to 10 cm deep.

denotes the velocity of EM waves in air (0.3 m/ns). Considering the case of nonmagnetic soil with low electrical conductivity, in the range of 10 MHz–1 GHz, the real part dominates the imaginary part of the dielectric permittivity, and neglecting Debye effect [*Debye*, 1929], equation (5) reduces to:

$$v = \frac{c}{\sqrt{\varepsilon'}} \ . \qquad (6)$$

We used this equation to compute the travel time of an EM wave through a layer of soil of known thickness with a known dielectric permittivity.

2.5. Electromagnetic Modeling

Numerous techniques are available for simulating GPR data, such as ray-based methods [e.g., *Cai and McMechan*, 1995; *Sethian and Popovici*, 1999], time-domain finite-difference full-waveform methods [e.g., *Kunz and Luebbers*, 1996; *Kowalsky et al.*, 2001], or Finite-Differences Time Domain (FDTD) [e.g., *Irving and Knight*, 2006]. We used the GprMax2D codes [*Giannopoulos*, 2005], which uses FDTD modeling to solve the Maxwell's equations in two dimensions.

3. Materials and Methods

3.1. Experimental Setup

We studied the infiltration of a 5 cm thick water layer inside a single ring infiltrometer in a sandy soil. The scheme of the apparatus is presented in Figure 1. The single ring infiltrometer was a 1 mm thick aluminum cylinder with a 60 cm diameter, approximately 20 cm high, buried in the soil to a depth of 10 cm. GPR antennae (namely the transmitter T and the receiver R) were set up in the middle of the ring. In all our field experiments, we used a Malå RAMAC system with shielded top antennae centered at 1600 MHz. The inner part of the cylinder was covered with a plastic waterproof sheet. This allowed us to fill the cylinder with water and create an initial 5 cm thick water layer, while preventing infiltration into the sand before starting data acquisition. The beginning of the GPR acquisition was launched when pulling away the plastic sheet to trigger water infiltration. A picture of the experiment is presented in Figure 2, where we see the cylinder filled with water, the 1.6 GHz antennae in the middle, a tank with a water level controller to maintain a constant water depth. The GPR system was set to acquire a trace every 10 s. With this apparatus, we conducted two types of infiltration: (i) a falling head infiltration, consisting of pulling away the plastic sheet and allowing water to infiltrate into the sand freely without adding water and (ii) a constant head infiltration, when water was continuously

Figure 2. Picture of the experiment. Ring infiltrometer filled with 5 cm of water, the 1.6 GHz antennae are in the middle protected from water by a plastic cover. We used a water level controller coupled with a tap-tank to maintain the 5 cm of water.

added to the ring to maintain a 5 cm depth of water layer during the infiltration experiment. In all GPR field data presented below, we subtracted the average trace and applied an Automatic Gain Control (AGC) to better resolve the reflection from the wetting front. Using only the arrival time of the reflections, there is no need to gain the data with relative amplitude conservation.

Field experiments took place in a quarry of sand in Cernay-La-Ville (Yvelines, France). The soil was a Fontainebleau sand composed of 99% quartz. Nine soil samples of known volume were extracted using a manual auger every 10 cm down to 80 cm. The laboratory analysis of these samples indicated that their average porosity was 0.43. Their average particle density was 2.48 ± 0.03 g cm^{-3}. Granulometric analysis showed that 10% of the grains had a diameter less than 0.125 mm and 86% less than 0.16 mm. These values are typical for Fontainebleau sand.

The M-vG parameters α, n, θ_s, θ_r of the sand were determined in parallel in the laboratory by several classical hanging water column experiments [*Dane and Hopmans*, 2002], however the λ parameter was not measured in laboratory and set to its typical value of 0.5, according to *Mualem* [1976]. The soil was considered homogeneous. Its initial water content, θ_i, and porosity, ϕ, were determined using gravimetric measurements of field samples (Table 2).

We also carried out disk infiltrometer experiments, using the multipotential method [*Ankeny et al.*, 1991; *Reynolds and Elrick*, 1991]. We obtained a value of the saturated hydraulic conductivity of $K_s = 0.108 \pm 0.01$ cm/min.

3.2. Modeling

Infiltration experiments were simulated by solving Richards' equation (equation (1)) using HYDRUS-1D [*Simunek and van Genuchten*, 1996; *Simunek et al.*, 2008]. The soil profile was 50 cm deep, assumed to be homogeneous, and divided into 1001 layers. We used either an atmospheric Boundary Condition (BC) with no rain and evaporation at the soil surface, for the falling head infiltration, or a constant pressure head of 5 cm at the top node, for the constant head infiltration. For both cases, a free drainage BC at the bottom of the soil profile was allowed. To simulate the 5 cm layer of water, the initial condition was set to 5 cm pressure head at the top node. We simulated the first 10 min of the experiment with a time step of 10 s, i.e., with 60 water content snapshots. Using the CRIM relation (equation (4)), each water content snapshot was converted to permittivity profiles (made of 1001 points), considering a three-phase media of sand, water, and air. These permittivity profiles were the input for the GprMax2D program simulating radargrams of the infiltration process. We then picked the maximum amplitude of the signal from the radargrams to obtain the Two-Way Travel time (TWT) of the wetting front reflection.

3.3. Inversion Algorithm
3.3.1. Convolution Algorithm

Our inversion algorithm was based on the comparison between TWT of the wetting front reflection observed from the radargrams acquired during the water infiltration experiment and the arrival times of these reflections computed from the water content profiles modeled by HYDRUS-1D. If a suitable relationship between water content and dielectric permittivity is known, water content profiles obtained by the resolution of the Richards' equation (done by HYDRUS-1D in our case) can be transformed to a 1-D series of reflection coefficients:

$$R_{i,t} = \frac{\sqrt{\varepsilon_{i+1,t}} - \sqrt{\varepsilon_{i,t}}}{\sqrt{\varepsilon_{i+1,t}} + \sqrt{\varepsilon_{i,t}}} \quad , \tag{7}$$

where $\varepsilon_{i,t}$ and $\varepsilon_{i+1,t}$ are the relative dielectric permittivities at the infiltration time t for two successive model cells centered at depth z_i and z_{i+1}. This reflection coefficient is only valid in the case of zero-offset source-receiver setup. The effective depth where the reflection coefficient is calculated is $z_R = \frac{z_i + z_{i+1}}{2}$. Knowing the dielectric permittivity of each layer of the profile, the electromagnetic wave velocity (equation (6)) and travel time can be computed. The travel time is used to interpolate reflection coefficients to a constant sampling rate. We compute a Ricker wavelet signal with the same time sampling. The central frequency of the Ricker wavelet was set to 1000 MHz, the same as the GPR signal recorded on the field. We differentiated it
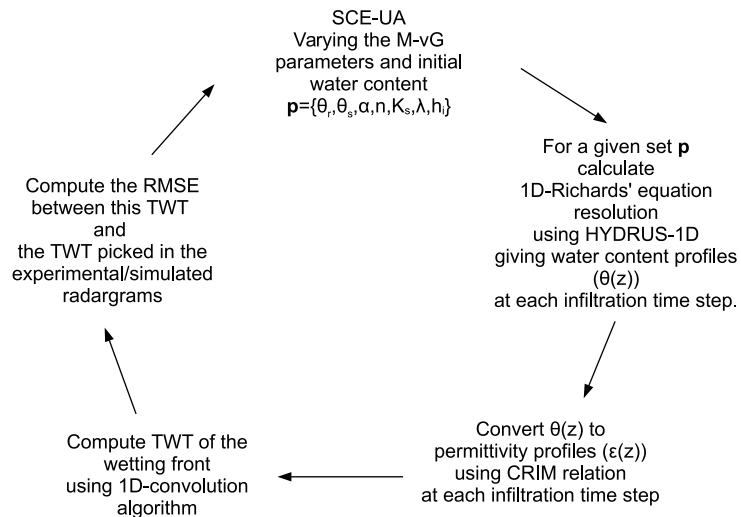
LÉGER ET AL.   5463

SCE-UA
Varying the M-vG
parameters and initial
water content
p={θ$_r$,θ$_s$,α,n,K$_s$,λ,h$_i$}

For a given set **p**
calculate
1D-Richards' equation
resolution
using HYDRUS-1D
giving water content profiles
(θ(z))
at each infiltration time step.

Compute the RMSE
between this TWT
and
the TWT picked in the
experimental/simulated
radargrams

Compute TWT of the
wetting front
using 1D-convolution
algorithm

Convert θ(z) to
permittivity profiles (ε(z))
using CRIM relation
at each infiltration time step

Figure 3. Flow diagram of the inversion procedure. "SCE-UA": Shuffled Complex Algorithm, "M-vG": Mualem-van Genuchten, "CRIM": Complex Refractive Index Method, "TWT": Two-Way Travel time, "RMSE": Root Mean Squared Error.

twice with respect to time to simulate the transformation made by the emitter and the receiver antennae. We then performed the convolution between this pseudo-GPR signal and the reflectivity to obtain:

$$O(t) = R(t) * \frac{\partial^2}{\partial t^2} I(t),$$ (8)

where $O(t)$ is the output signal, $R(t)$ is the reflectivity, and $I(t)$ is the input source of the antenna. The TWT corresponding to the absolute maximum of $O(t)$ was used as the wetting front reflection TWT. For inversion, we used this 1-D convolution algorithm to determine the wetting front TWT, being less time consuming than 2D-FDTD. TWT computed with those two methods are compared in the following.

3.3.2. Inversion Modeling Procedure

We used the TWT obtained from the radargram (modeled or experimental) as data to be fitted to derive the set of M-vG parameters, $\{ \theta_r,\ \theta_s,\ \alpha,\ n,\ K_s,\ \lambda \}$ and the initial water content, θ_i which will be stated as the parameter vector: $p=\{ \theta_r,\ \theta_s,\ \alpha,\ n,\ K_s,\ \lambda, \theta_i \}$. This set of parameters is estimated using the Shuffled Complex Evolution (SCE-UA) algorithm, by minimizing the objective function expressed as the Root Mean Square Error (RMSE) between the modeled and experimental TWT of the wetting front reflection.

Using Hydrus-1D, we generated 60 water content snapshots for every 10 s using the set of input parameters p. For each generated parameter set p, we calculated the TWT using our 1-D convolution algorithm and we computed the RMSE between these times and the data as an objective function. This inversion modeling procedure is presented as a flow diagram in Figure 3. The optimal set of parameters p_{op} corresponds to the minimum of the objective function.

4. Falling Head Infiltration Experiment

4.1. Numerical Example
4.1.1. Forward Modeling

The set of hydraulic parameters used for this numerical example is presented in Table 1, as p_{in}. The permittivity profiles, resulting from water content conversions from HYDRUS-1D to permittivity and which were used as input for the GprMax2D program, are presented in Figure 4a. The simulated GPR monitoring of the infiltration process is shown in Figure 4b. The horizontal axis is the infiltration time, two traces being separated by 10 s, as permittivity profiles are. The vertical axis is the TWT of the EM wave coming back to the receiver.

On the profile presented in Figure 4b, we denote one particular reflection, labeled A. Its arrival time is increasing as the wetting front moves deeper. This reflection is interpreted as coming from the wetting

LÉGER ET AL.
5464

Table 1. Hydraulic Parameters for the Numerical Experiments[a]

	θ_r (cm³ cm⁻³)	θ_s (cm³ cm⁻³)	α (cm⁻¹)	n	K_s (cm/min)	λ	θ_i (cm³ cm⁻³)	log_{10}(RMSE) (log_{10}(ns))
p_{in}	0.06	0.39	0.023	6.71	0.120	0.5	0.07	
Falling Head Infiltration								
p_{op}	0.062	0.396	0.0226	6.614	0.119	0.444	0.076	−7.15
$\left\|\frac{p_{op}-p_{in}}{p_{in}}\right\|$	3.3%	1.5%	1.7%	1.4%	0.8%	11%	9%	
Constant Head Infiltration								
p_{op}	0.043	0.388	0.0215	6.97	0.118	0.457	0.053	−7.86
$\left\|\frac{p_{op}-p_{in}}{p_{in}}\right\|$	28%	0.5%	7%	3.9%	1.7%	8.6%	24%	

[a]p_{in} is the set of parameters used as input to generate the radargrams presented in Figures 4b and 7b. p_{op} is the set of parameters optimized by the SCE-UA global optimizer.

front. The reflections labeled A' and A'' are primary and secondary multiples of reflection A. The reflection labeled B is the direct air-ground wave. After 7 min, the 5 cm layer of water has been infiltrated, and drainage is starting. As a consequence, the permittivity of the upper part of the medium decreases and the velocity increases (equation (6)). The TWT of reflection A increases more slowly, creating a change of slope in the reflection time curve (Figure 4b). In Figure 4c, we display the TWT of the maximum peak of reflection A (obtained from Figure 4b) and the TWT calculated from the convolution algorithm using the input parameter set, p_{in}. In Figure 4d, we display time differences between these two curves. It has to be precised that
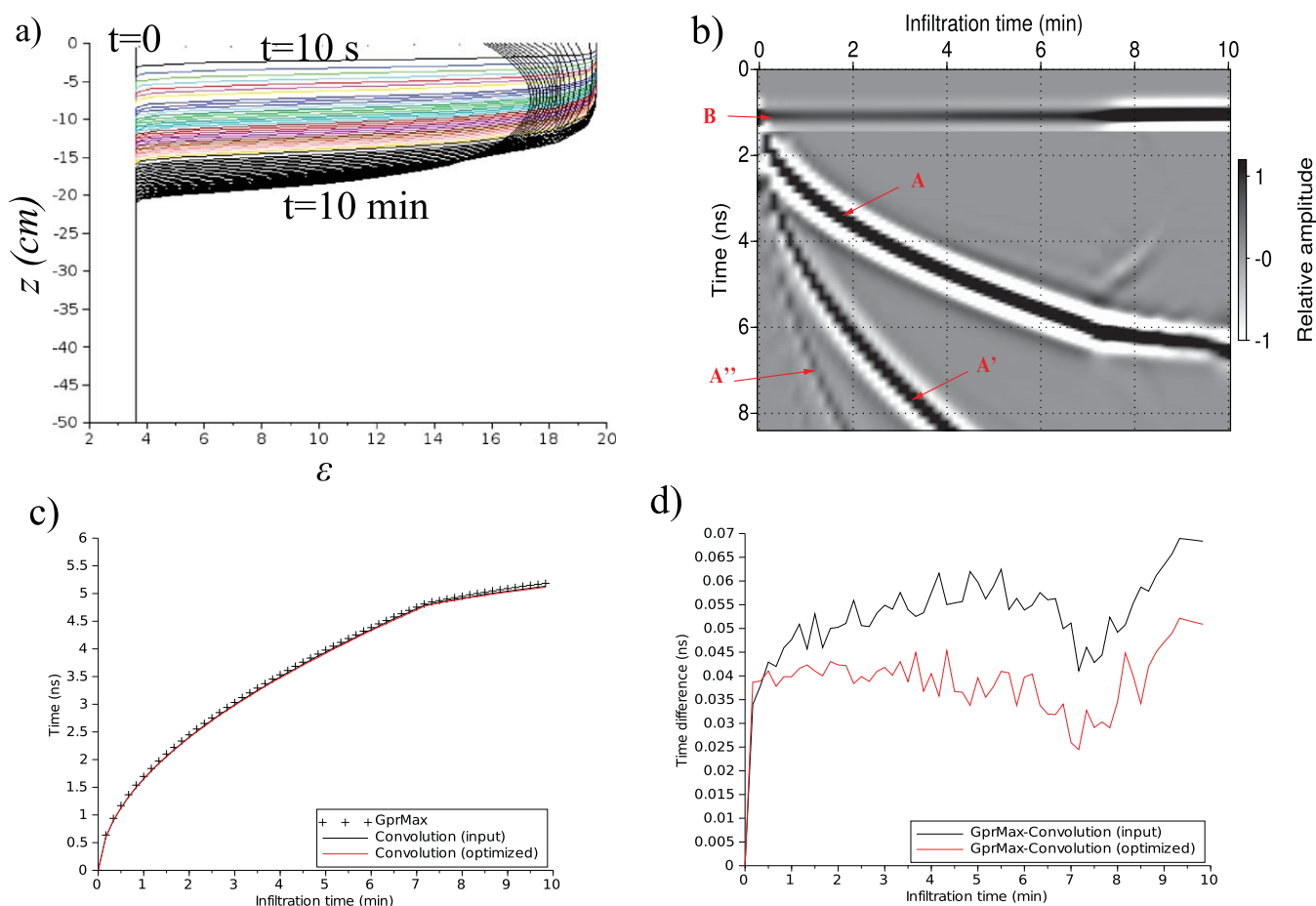

Figure 4. Numerical example of a falling head infiltration: (a) permittivity profiles (curves are plotted every 10 s), (b) radargram simulated with GprMax 2D (reflection A is coming from the wetting front, B is the direct wave, A′ and A″ are multiples of reflection A, (c) comparison between TWT obtained by: crosses, picking reflection A peaks on radargram (Figure 4b), black line, using the convolution algorithm with p_{in}, red line, using the convolution algorithm with p_{op}. (d) Differences between the TWT using: black line, the convolution algorithm with p_{in} and the radargram (Figure 4b), red line, the convolution algorithm with p_{op} and the radargram (Figure 4b).

Table 2. Hydraulic Parameters for the Field Experiments[a]

	Date	θ_r (cm^3 cm^{-3})	θ_s (cm^3 cm^{-3})	α (cm^{-1})	n	K_s (cm min^{-1})	λ	θ_i (cm^3 cm^{-3})	θ_i^* (cm^3 cm^{-3})	log_{10}(RMSE) (log_{10}(ns))
Falling Head Infiltration										
p_{op}^1	27 Jan 2012	0.044	0.38	0.021	6.01	0.11	0.45	0.08	0.092*	−4.81
p_{op}^2	25 May 2011	0.036	0.405	0.0118	7.77	0.022	0.33	0.29	0.09*	−3.18
p_{op}^3	1 Jun 2011	0.067	0.389	0.036	8.6	0.034	0.31	0.067	0.09*	−4.73
p_{op}^4	7 Nov 2012	0.021	0.429	0.0208	5.82	0.0235	0.42	0.04	0.15*	−4.67
p_{op}^5	7 Nov 2012	0.051	0.373	0.022	5.73	0.024	0.69	0.07	0.15*	−4.96
Constant Head Infiltration										
p_{op}^6	25 Jul 2013	0.057	0.36	0.039	5.95	0.33	0.36	0.058	0.054*	−5.61
p_{op}^7	22 Feb 2013	0.05	0.387	0.0144	5.75	0.029	0.37	0.22	0.067*	−4.52
p_{op}^8	25 Jul 2013	0.051	0.413	0.024	7.11	0.129	0.482	0.056	0.054*	−7.64
Laboratory and Field Measurements										
p_{cla}	7 Nov 2012	0.06	0.39	0.023	6.71	0.108*	0.5**			

[a]The single asterisk indicates values obtained from external field measurements such as disk infiltrometer experiment for K_s and gravimetric measurements from field samples for θ_i. The double asterisks indicate that we set this value to 0.5 according to *Mualem* [1976]. p_{cla} is formed by the M-vG parameters determined by water hanging column experiments and the K_s value obtained from the disk infiltrometer data. p_{op}^{1-8} are the set of parameters inverted by our method.

the TWT of the absolute maximum peak of the direct wave (noted *B* in Figure 4b) is subtracted from all TWT.

In Figures 4b and 4c, we see that GprMax picking and the convolution algorithm, for the p_{in} set are in agreement. The maximum time difference is less than 0.07 ns, showing that the convolution algorithm is accurate enough, even though the time step in the FDTD data is 0.01 ns.

4.1.2. Inverse Modeling
We used the TWT obtained from the radargram of Figure 4b (crosses in Figure 4c) as data to be fitted to derive the set of M-vG parameters and the initial water content $p_{op}=\{\theta_r,\ \theta_s,\ \alpha,\ n,\ K_s,\ \lambda, \theta_i\}$ using the inversion procedure shown in Figure 3. The RMSE was minimized for the following set $p_{op}=\{\theta_r=0.062\,\text{cm}^3/\text{cm}^3, \theta_s=0.396\ \text{cm}^3/\text{cm}^3, \alpha=0.0226\,\text{cm}^{-1}, n=6.614, K_s=0.119\,\text{cm/min}, \lambda=0.444, \theta_i=0.076\,\text{cm}^3\,\text{cm}^{-3}\}$, which has to be compared with the input set values, i.e., $p_{in}=\{\ \theta_r=0.06\,\text{cm}^3/\text{cm}^3, \theta_s=0.39\,\text{cm}^3/\text{cm}^3, \alpha=0.023\,\text{cm}^{-1}, n=6.71, K_s=0.12\,\text{cm/min}, \lambda=0.5, \theta_i=0.07\,\text{cm}^3\text{cm}^{-3}\}$. Table 1 presents both sets p_{in} and p_{op} and the relative differences between them. The differences between these two sets of parameters are small considering that one is obtained using a straight 1-D convolution algorithm to invert 2D-FDTD simulated data. The comparisons between the simulated radargram picking of the wetting front (obtained from Figure 4b) and the TWT calculated by the convolution algorithm with the inverted set of parameters p_{op} is presented in Figure 4c and time differences in Figure 4d. This inversion of a synthetic example validates our 1-D convolution algorithm coupled with SCE-UA global optimization to invert experimental results, modeled with GprMax2D, to obtain the M-vG parameters and the initial water content of the considered soil.

4.2. Field Experiment
4.2.1. Experimental Data and Their Analysis
Five falling head experiments took place in the quarry of Fontainebleau sand described in section 3.1. For each experiment, the initial volumetric water content was determined by gravimetric measurements on several soil core samples (Table 2).

As an example of the field GPR data, the radargram acquired on the 27 January 2012 is shown in Figure 5. During this experiment, the 5 cm water layer was fully infiltrated after about 10 min, although in certain areas of the soil surface this time has been slightly shorter. The profile in Figure 5 shows three distinctive reflections. The one interpreted as coming from the infiltration front, labeled *A*, has an arrival time varying from 0 ns down to 7 ns. The other reflections come from the cylinder and are interpreted in *Léger and Saintenoy* [2012]. We did not use them in the present work. We determined the TWT of the *A* reflection peak and inverted the set of parameters using the same algorithm as for the synthetic case, summarized in the flow diagram (Figure 3). The time zero was set to the TWT of the direct wave peak, which corresponds to the TWT of the wetting front reflection for the first trace. The set of parameter, p_{op}^1, minimizing the objective function is presented in Table 2.

In Figure 6a, we compare the TWT of the wetting front obtained from (i) the modeling using the set of parameters p_{cla}, formed by the M-vG parameters determined by water hanging column experiments and
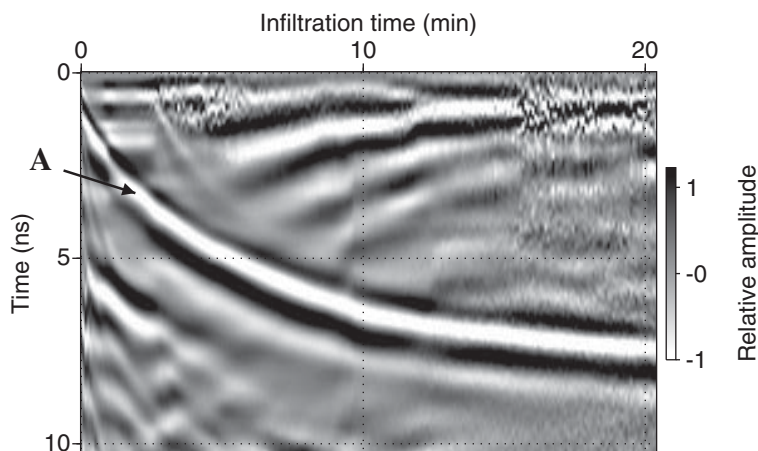
Figure 5. GPR data acquired during a falling head infiltration (field experiment of the 27 January 2012). Reflection A is the reflection coming from the wetting front.

the K_s value obtained from the disk infiltrometer data, (ii) the modeling using the optimized set of parameters p_{op}^1, and (iii) reflection A in the experimental radargram (Figure 5).

In addition, Table 2 presents four other experimental results performed in the same quarry but at different sites and during other days. The inverted sets p_{op}^2 to p_{op}^5 were all determined with the same procedure as p_{op}^1 with 10 min of GPR monitoring or less.

The last three experiments in Table 2, labeled p_{op}^{3-5} and presented in Figures 6c–6e, show that the M-vG parameters determined by laboratory measurements and disk infiltrometer test do not lead to a TWT close to the experimental GPR picking. This variability will be discussed in section 6.

The second inversion, labeled p_{op}^2, seems accurate in Figure 6b but leads to a α value lower than in the other cases. It is correlated to the higher inverted initial water content, $\theta_i = 0.29\, \mathrm{cm}^3/\mathrm{cm}^{-3}$, because of relation equation (2). The first minute of the infiltration is poorly fitted by the optimized model. We suspect that the sampling measurement (one trace every 10 s) was too large to get accurate measurements, especially at the beginning of the infiltration, not well resolved, leading to a shift between the generated and the experimental TWT.

5. Constant Head Infiltration Experiment

5.1. Numerical Example
5.1.1. Forward Modeling
For this second case, a water layer of 5 cm above the ground was kept constant during the entire experiment. As above, using the same set of parameters p_{in} as in the first synthetic example (Table 1), we modeled infiltration of water inside a ring infiltrometer by applying a constant pressure head of 5 cm to the top node during 10 min. The permittivity profiles are presented in Figure 7a, with each curve plotted every 10 s as in the falling head case. Figure 7b shows the radargram simulated with GprMax2D. As can be seen, the reflection labeled A corresponds to the infiltration front reflection. Its TWT is increasing with no change in slope because infiltration is being constantly fed by constant ponding, contrary to the previous falling head case. In Figure 7c, we computed the TWT of the wetting front using the convolution algorithm and compare them to the picked TWT of reflection A from the radargram in Figure 7b. Time differences between these two curves (black line in Figure 7d) are less than 0.07 ns as in the former synthetic example.

5.1.2. Inverse Modeling
We inverted the whole set of parameters p_{op}, by minimizing the differences between the arrival times of the wetting front reflection obtained by the convolution algorithm and the arrival times picked from the simulated radargram in Figure 7b. The objective function was minimized for the set $p_{op} = \{\theta_r = 0.043\, \mathrm{cm}^3/\mathrm{cm}^3, \theta_s = 0.388\, \mathrm{cm}^3/\mathrm{cm}^3, \alpha = 0.0215\, \mathrm{cm}^{-1}, n = 6.973, K_s = 0.118\, \mathrm{cm}/\mathrm{min}, \lambda = 0.457, \theta_i = 0.053\, \mathrm{cm}^3\mathrm{cm}^{-3}\}$,
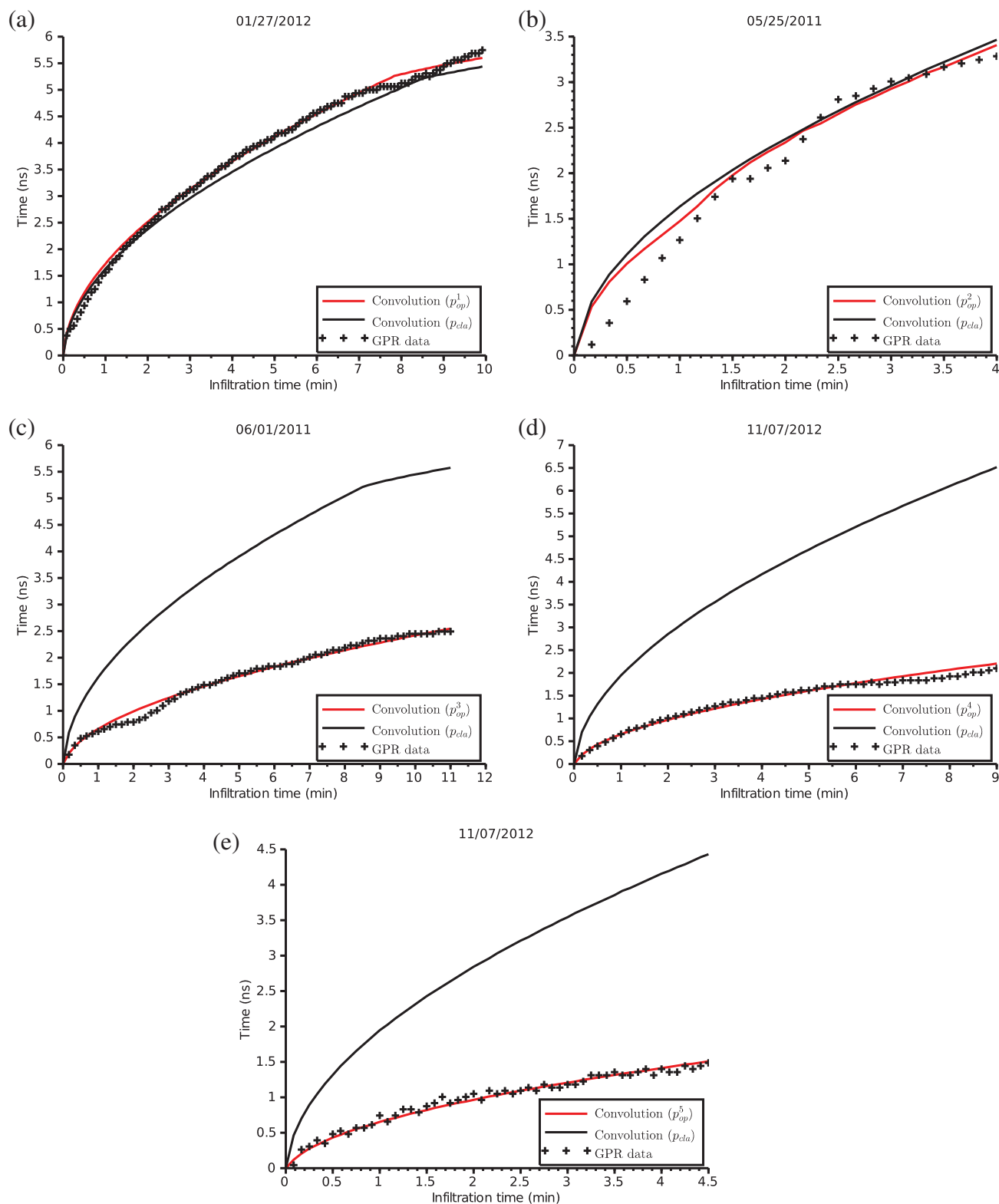
Figure 6. For the five falling head infiltration field experiments: comparisons of TWT from the wetting front obtained (i) from reflection A in the experimental radargrams, (ii) with modeling using p_{cla} (Table 2), and (iii) with modeling using (a) p_{op}^1, (b) p_{op}^2, (c) p_{op}^3, (d) p_{op}^4, and (e) p_{op}^5.
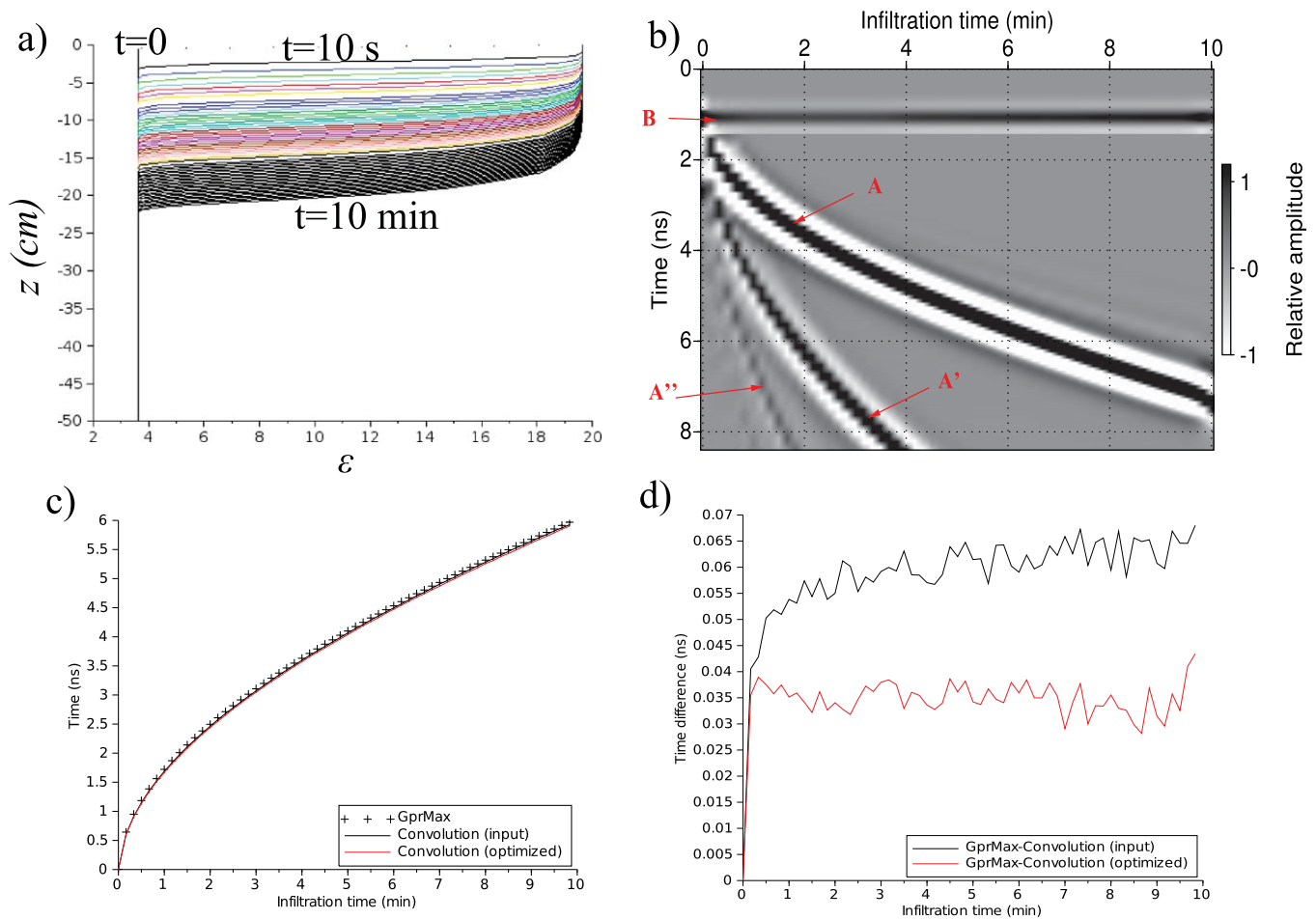
Figure 7. Numerical example of a constant head infiltration: (a) permittivity profiles (curves are plotted every 10 s), (b) radargram simulated with GprMax 2D (reflection A is coming from the wetting front, B is the direct wave, A' and A'' are multiples of reflection A, (c) comparison between TWT obtained by, crosses, picking reflection A peaks on radargram (Figure 7b), black line, using the convolution algorithm with p_{in}, red line, using the convolution algorithm with p_{op}. (d) Differences between the TWT using: black line, the convolution algorithm with p_{in} and the radargram (Figure 7b), red line, the convolution algorithm with p_{op} and the radargram (Figure 7b).

which is close to the values used as input for simulating the data, p_{in}, as in the former falling head case. Table 1 presents the relative differences between the parameters set as input and the optimal parameters. The comparisons between the simulated radargram picking of the wetting front (obtained from Figure 7b) and the TWT calculated by the convolution algorithm with the inverted set of parameters p_{op} is presented in Figures 7c and 7d. This synthetic inversion validates our 1-D convolution algorithm coupled with SCE-UA global optimization to invert experimental data to obtain M-vG parameters and the initial water content in the case of constant head infiltration experiment.

5.2. Field Experiments

Three experiments took place in the same quarry of Fontainebleau sand as in the previous experiments. The GPR data obtained on the 25 July 2013 are shown in Figure 8. In this profile, the TWT of reflection *A* increases from 0 to about 9 ns after 9.5 min of infiltration. We picked the arrival time of the *A* reflection peak and computed the objective function using the same procedure as described before. We obtained the minimum of the objective function for the set $p_{op}^6 = \{\theta_r = 0.057 \text{ cm}^3\text{cm}^{-3}, \theta_s = 0.36 \text{ cm}^3\text{cm}^{-3}, \alpha = 0.039 \text{ cm}^{-1}, n = 5.95, K_s = 0.33 \text{ cm min}^{-1}, \lambda = 0.36, \theta_i = 0.058 \text{ cm}^3\text{cm}^{-3}\}$, as summarized in Table 2. Again, these values should be compared to those obtained by the disk infiltrometer and water hanging column experiments, p_{cla}, and to other sets of parameters optimizing data acquired on this soil during this study.
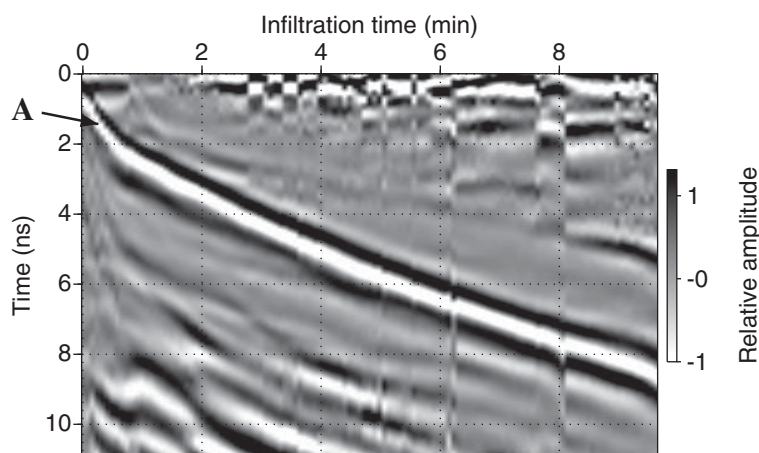
Figure 8. GPR data acquired during a constant head infiltration (field experiment of the 25 July 2013). Reflection A is the reflection coming from the wetting front.

In Figure 9, we display the TWT of the wetting front obtained from (i) the modeling using the set of parameters p_{cla}, (ii) the modeling using the optimized set of parameter p_{op}^{6-7-8}, and (iii) the experimental radargrams. From Figure 9, we can see that our algorithm is accurate and able to differentiate between close values of hydraulic parameters. As in the third experiment (Figure 6c), it shows that the M-vG parameters determined by laboratory measurements and disk infiltrometer test p_{cla} do not lead to a TWT close to the experimental GPR picking.

Once again, despite its good fitting in Figure 9b, the second constant head experiment (p_{op}^{7}) has a low α value and high inverted initial water content, $\theta_i = 0.22\,\text{cm}^3\text{cm}^{-3}$. Picking or poor sampling might not be the source of error. We see around 1 min of infiltration a change in slopes in the TWT, due to a small issue in the constant head device. We suspect this change is responsible for this low value of α.

Concerning Figure 9c, the GPR data are not fitted correctly, despite the fact the optimized set of parameters p_{op}^{7} is consistent with the other experiments.

6. Discussion

The results presented above indicate clearly that a commercial surface GPR can be used as a tool for monitoring the wetting front in sand soils. Although the use of surface-based GPR data to estimate the parameters of unsaturated flow models is not new [*Moysey*, 2010], our method gives in a single experiment accurate values of all the M-vG parameters $\{\,\theta_r,\ \theta_s,\ \alpha,\ n,\ K_s,\ \lambda\,\}$ and the initial volumetric water content θ_i, comparable to those obtained with disk infiltrometer and water hanging column measurements, and relevant in the case of sand soil. A distinct advantage of our approach is the simplicity of the algorithm and its quick convergence, which is very encouraging for application to more complicated models (layered soils), and other soil types.

Although we obtained different values for the set of M-vG parameters in our different experiments they are consistent within each others and are expected for this type of Fontainebleau sand soils. Those differences arise mainly because the experiments were not done the same day nor on the same sites. The sites were decades meters away from each others, so that spatial variability can explain the observed differences between the estimated values. Heterogeneities in unsaturated hydraulic properties were studied and described on different soils in the works of *Russo and Bouton* [1992], *Chen et al.* [2012a, 2012b], and *Guadagnini et al.* [2013]. According to these studies, the variabilities observed in the M-vG parameters we inverted using our method are in the range of the spatial and temporal variabilities expected in such field studies.

That said, the discrepancies between hydraulic parameters determined by our GPR algorithm and the laboratory/disk infiltrometer measurements may come from different phenomena.
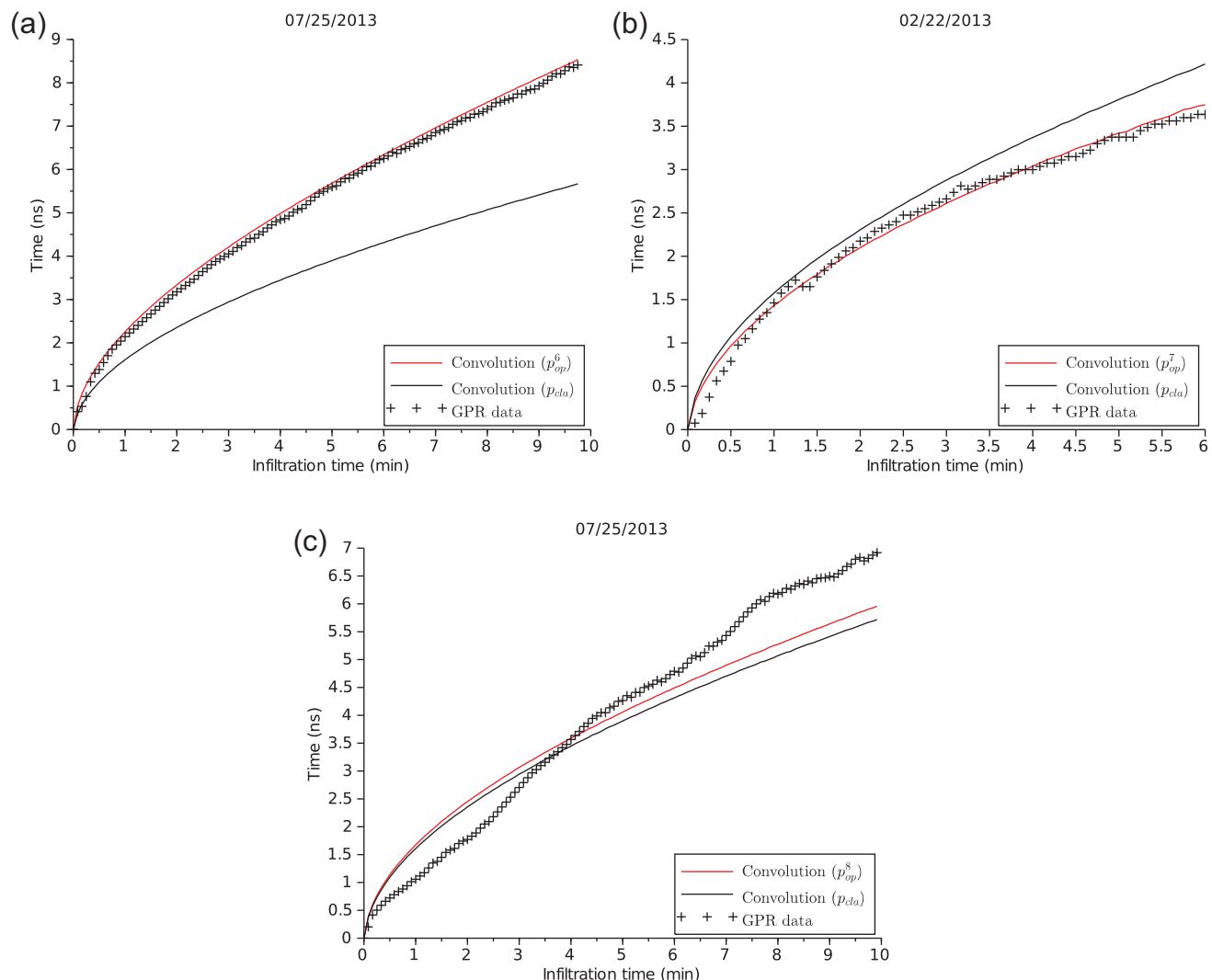
LÉGER ET AL.   5470

Figure 9. For the three constant head infiltration field experiments: comparisons of TWT from the wetting front obtained (i) from reflection *A* in the experimental radargrams, (ii) with modeling using p_{cla} (Table 2), and (iii) with modeling using (a) p_{op}^6, (b) p_{op}^7, and (c) p_{op}^8.

First of all, the M-vG parameters determined from the water hanging column experiment were obtained from a single drainage curve of reconstituted samples, whereas on the field, the infiltration is a ponded one, wetting front coming from the top.

Second, despite the fact that we upgraded the single ring infiltrometer by the use of GPR to monitor the wetting front, our experiments still suffer from the problem of entrapped air, which causes reduction of saturated water content and hydraulic conductivity and deviation of the other hydraulic parameters. This issue cannot be fixed with ponded infiltration. Disk infiltrometer measurement may cause less problems, working with negative pressure potentials [*Ankeny et al.*, 1991; *Reynolds and Elrick*, 1991].

During our modeling, we considered an homogeneous and isotropic soil. As we said, real soils exhibit heterogeneities, triggering preferential flows. Even in the case of Fontainebleau sand, differences in packing and compaction could lead to the creation of preferential flow paths. One of the ways to resolve this issue could be to use a dual porosity model [*Gerke and van Genuchten*, 1993] and a stochastic procedure to generate a high number of soil models with different parameters, and perform statistical analysis on the obtained set of parameters.

Some remarks are needed about the comparison between 1-D temporal convolution and the real electromagnetic signal. Our inversion algorithm is based on the assumption that soil can be represented as a stack

of homogeneous layers, and forces the reflection coefficient (equation (7)) to be expressed as a normal incidence case. Second, we considered that the 2-D plane waves computed by the FDTD algorithm (modeling) and 3-D plane waves (experiments) could be treated as a 1-D temporal convolution. This limitation will be studied in future works, using SWMS-2D [*Simunek et al.*, 1994] to simulate 2-D axi-symmetrical infiltration.

An other source of inevitable issue, working with GPR, arises from the dispersion of the electromagnetic signal because of the soil electrical conductivity. The penetration of the EM wave will decrease with increasing electrical conductivity, which clearly indicates the difficulty to work with high clay content soils.

Finally, the influence of the initial water content, θ_i, is of much importance because the power of the returned GPR signal is proportional to the permittivity difference between the saturated and the initial state of the soil. Higher contrast between those two will lead to better ability to monitor the wetting front.

7. Summary

This research investigated the use of on-ground surface GPR to monitor the wetting front during infiltration inside a ring infiltrometer. We showed by modeling and experiments that a standard GPR device was able to monitor the wetting front in a sandy soil. We tested on synthetic cases the ability of our algorithm to invert modeling and experimental data to obtain the M-vG parameters and the initial water content using a Shuffled Complex Algorithm optimization procedure. We presented results from eight field infiltration experiments. The experiments were falling head infiltrations and constant head infiltrations, performed in a quarry of Fontainebleau sand. Those two types of experiments correspond to transient and steady state infiltration, and show the ability of our method to work in both cases. The retrieved parameters were comparable to those obtained with laboratory and disk infiltrometer experiments, and were in agreement with the parameters expected for this type of sand soils. This new field method allowing to retrieve the M-vG parameters in a short amount of time, with no need of additional time-consuming laboratory measurements, is very promising, and further researches are currently carried out on other type of soils, particularly loessic soils.

References

Akbar, M., A. Kenimer, S. Searcy, and H. Tobert (2005), Soil water estimation using electromagnetic induction, *Trans. ASAE*, *48*(1), 129–135.

Angulo-Jaramillo, R., J.-P. Vandervaere, S. Roulier, J.-L. Thony, J.-P. Gaudet, and M. Vauclin (2000), Field measurement of soil surface hydraulic properties by disc and ring infiltrometers: A review and recent developments, *Soil Tillage Res.*, *55*(1), 1–29.

Ankeny, M. D., M. Ahmed, T. C. Kaspar, and R. Horton (1991), Simple field method for determining unsaturated hydraulic conductivity, *Soil Sci. Soc. Am. J.*, *55*(2), 467–470.

Annan, A. (1999), Ground Penetrating Radar: Workshop notes, *Tech. Rep. 402*, Sensors and Software Inc., Ont., Canada, Mississauga.

Annan, A. P. (2005), GPR methods for hydrogeological studies, in *Hydrogeophysics*, edited by Y. Rubin and S. S. Hubbard, pp. 185–213, Springer, Dordrecht, Netherlands.

Barati, R. (2011), Parameter estimation of nonlinear Muskingum models using Nelder-Mead Simplex algorithm, *J. Hydraul. Eng.*, *123*(2), 137–142.

Binley, A., P. Winship, R. Middleton, M. Pokar, and J. West (2001), High-resolution characterization of vadose zone dynamics using cross-borehole radar, *Water Resour. Res.*, *37*(11), 2639–2652.

Birchak, J., L. Gardner, J. Hipp, and J. Victor (1974), High dielectric constant microwave probes for sensing soil moisture, *Proc. IEEE*, *35*(1), 85–94.

Boivin, P., J. Touma, and P. Zante (1987), Mesure de l'infiltrabilité du sol par la méthode du double anneau. 1: Résultats expérimentaux, *Cah. ORSTOM, Sér. Pédol.*, *24*(1), 17–25.

Bradford, J. (2006), Applying reflection tomography in the post-migration domain to multi-fold Ground-Penetrating Radar data, *Geophysics*, *71*(1), K1–K7.

Bradford, J. H. (2008), Measuring water content heterogeneity using multifold GPR with reflection tomography, *Vadose Zone J.*, *7*(1), 184–193.

Busch, S., L. Weihermuller, J. Huisman, C. Steelman, A. Endres, H. Vereecken, and J. van der Kruk (2013), Coupled hydrogeophysical inversion of time-lapse surface GPR data to estimate hydraulic properties of a layered subsurface, *Water Resour. Res.*, *49*, 8480–8494, doi:10.1002/2013WR013992.

Cai, J., and G. A. McMechan (1995), Ray-based synthesis of bistatic Ground-Penetrating Radar profiles, *Geophysics*, *60*(1), 87–96.

Chen, J., S. Hubbard, and Y. Robin (2001), Estimating the hydraulic conductivity at the South Oyster site from geophysical tomographic data using Bayesian techniques based on the normal linear regression model, *Water Resour. Res.*, *37*(6), 1603–1613.

Chen, P.-Y., C.-H. Chen, N.-S. Hsu, C.-M. Wu, and J.-C. Wen (2012a), Influence of heterogeneity on unsaturated hydraulic properties. 1: Local heterogeneity and scale effect, *Hydrol. Processes*, *26*(23), 3593–3603.

Chen, P.-Y., C.-H. Chen, N.-S. Hsu, C.-M. Wu, and J.-C. Wen (2012b), Influence of heterogeneity on unsaturated hydraulic properties. 2: Percentage and shape of heterogeneity, *Hydrol. Processes*, *26*(23), 3604–3613.

Childs, E. C., and N. Collis-George (1950), The permeability of porous materials, *Proc. R. Soc. London, Ser. A*, *201*(1066), 392–405.

Clothier, B., and I. White (1981), Measuring sorptivity and soil water diffusivity in the field, *Soil Sci. Soc. Am. J.*, *45*(2), 241–245.

Dagenbach, A., J. Buchner, P. Klenk, and K. Roth (2013), Identifying a parametrisation of the soil water retention curve from on-ground GPR measurements, *Hydrol. Earth Syst. Sci.*, *17*(1), 611–618.

Dane, J. H., and J. W. Hopmans (2002), Hanging water column, in *Method of Soil Analysis. Part 4: Physical Methods*, edited by J. H. Dane and G. C. Topp, pp. 680–684, Soil Sci. Soc. of Am., Inc., Madison, Wis.

Debye, P. (1929), *Polar Molecules*, Dover, N. Y.

Doolittle, J., B. Jenkinson, D. Hopkins, M. Ulmer, and W. Tuttle (2006), Hydropedological investigations with Ground-Penetrating Radar (GPR): Estimating water-table depths and local ground-water flow pattern in areas of coarse-textured soils, *Geoderma*, *131*, 317–329.

Duan, Q., S. Sorooshian, and V. Gupta (1992), Effective and efficient global optimization for conceptual rainfall-runoff models, *Water Resour. Res.*, *28*(4), 1015–1031.

Endres, A., J. Jones, and E. Bertrand (2007), Pumping-induced vadose zone drainage and storage in an unconfined aquifer: A comparison of analytical model predictions and field measurements, *J. Hydrol.*, *335*(1–2), 207–218.

Evett, S., and G. Parkin (2005), Advances in soil water content sensing: The continuing maturation of technology and theory, *Vadose Zone J.*, *4*(4), 986–991.

Gerke, H., and M. T. van Genuchten (1993), A dual porosity model for simulating the preferential movement of water and solutes in structured porous media, *Water Resour. Res.*, *29*(2), 305–319.

Giannopoulos, A. (2005), Modelling Ground-Penetrating Radar by GprMax, *Construction Building Mater.*, *19*(10), 755–762.

Goyal, V., P. Gupta, S. Seth, and V. Singh (2006), Estimation of temporal changes in soil moisture using resistivity method, *Hydrol. Processes*, *10*(9), 1147–1154.

Greaves, R., D. Lesmes, J. Lee, and M. Toksöz (1996), Velocity variations and water content estimated from multi-offset Ground-Penetrating Radar, *Geophysics*, *61*(3), 683–695.

Grote, K., S. Hubbard, and Y. Rubin (2002), GPR monitoring of volumetric water content in soils applied to highway construction and maintenance, *Leading Edge*, *21*(5), 482–504.

Guadagnini, A., S. Neuman, M. Schaap, and M. Riva (2013), Anisotropic statistical scaling of vadose zone hydraulic property estimates near Maricopa, Arizona, *Water Resour. Res.*, *49*, 8463–8479, doi:10.1002/2013WR014286.

Haarder, E., M. L. K. Jensen, and L. Nielsen (2011), Visualizing unsaturated flow phenomena using high-resolution reflection Ground Penetrating Radar, *Vadose Zone J.*, *10*(1), 84–97.

Huisman, J., S. Hubbard, J. Redman, and A. Annan (2003), Measuring soil water content with Ground-Penetrating Radar, *Vadose Zone J.*, *2*(4), 476–491.

Huyer, W., and A. Neumaier (1999), Global optimization by multilevel coordinate search, *J. Global Optim.*, *4*(14), 331–355.

Irving, J., and R. Knight (2006), Numerical modeling of Ground-Penetrating Radar in 2D using Matlab, *Comput. Geosci.*, *32*(9), 1247–1258.

Jadoon, K., L. Weihermüller, B. Scharnagl, M. Kowalsky, M. Bechtold, S. Hubbard, H. Vereecken, and S. Lambot (2012), Estimation of soil hydraulic parameters in the field by integrated hydrogeophysical inversion of time-lapse Ground-Penetrating Radar, *Vadose Zone J.*, *11*(4), doi:10.2136/vzj2011.0177.

Klotzsche, A., J. van der Kruk, N. Linde, J. Doetsch, and H. Vereecken (2013), 3D characterization of high-permeability zones in a gravel aquifer using 2D crosshole GPR full-waveform inversion and waveguide detection, *Geophys. J. Int.*, *195*(2), 932–944.

Kosugi, K., J. Hopmans, and J. Dane (2002), *Parametric models, in* Methods of Soil Analysis. Part 4: Physical Methods, edited by J. H. Dane and G. C. Topp, pp. 739–755, Soil Sci. Soc. Am., Inc., Madison, Wis.

Kowalsky, M., P. Dietrich, G. Teutsch, and Y. Rubin (2001), Forward modeling of Ground-Penetrating Radar using digitized outcrop images and multiple scenarios of water saturation, *Water Resour. Res.*, *37*(6), 1615–1626.

Kowalsky, M., S. Finsterle, J. Peterson, S. Hubbard, Y. Rubin, E. Majer, A. Ward, and G. Gee (2005), Estimation of field-scale soil hydraulic and dielectric parameters through joint inversion of GPR and hydrological data, *Water Resour. Res.*, *41*, W11425, doi:10.1029/2005WR004237.

Kunz, K., and R. Luebbers (1996), *The Finite Difference Time Domain Method for Electromagnetics*, CRC Press, Boca Raton, Fla.

Lagarias, J. C., J. A. Reeds, M. H. Wright, and P. E. Wright (1998), Convergence properties of the Nelder–Mead simplex method in low dimensions, *SIAM Journal on Optimiziation*, *9*(1), 112–147, doi:10.1137/S1052623496303470.

Lai, W., W. Tsang, H. Fang, and D. Xiao (2006), Experimental determination of bulk dielectric properties and porosity of porous asphalt and soils using GPR and a cyclic moisture variation technique, *Geophysics*, *71*(4), K93–K102.

Lai, W., S. Kou, and C. Poon (2012), Unsaturated zone characterization in soil through transient wetting and drying using GPR joint time-frequency analysis and grayscale images, *J. Hydrol.*, *452–453*, 1–13.

Lambot, S., M. Javaux, F. Hupet, and M. Vanclooster (2002), A global multilevel coordinate search procedure for estimating the unsaturated soil hydraulic properties, *Water Resour. Res.*, *38*(11), 1224, doi:10.1029/2001WR001224.

Lambot, S., E. Slob, M. Vanclooster, and H. Vereecken (2006), Closed loop GPR data inversion for soil hydraulic and electric property determination, *Geophys. Res. Lett.*, *33*, L21405, doi:10.1029/2006GL027906.

Lambot, S., E. Slob, J. Rhebergen, O. Lopera, K. Jadoon, and H. Vereecken (2009), Remote estimation of the hydraulic properties of a sand using full-waveform integrated hydrogeophysical inversion of time-lapse, off ground GPR data, *Vadose Zone J.*, *8*(3), 743–754.

Léger, E., and A. Saintenoy (2012), Surface Ground-Penetrating Radar monitoring of water infiltration inside a ring infiltrometer, in *14th International Conference on Ground Penetrating Radar (GPR)*, edited by IEEE, pp. 680–683, IEEE, Shanghai, China.

Lunt, I., S. Hubbard, and Y. Rubin (2005), Soil moisture content estimation using Ground-Penetrating Radar reflection data, *J. Hydrol.*, *307*(1–4), 254–269.

Mangel, A., S. Moysey, J. Ryan, and J. Tarbutton (2012), Multi-offset Ground-Penetrating Radar imaging of a lab-scale infiltration test, *Hydrol. Earth Syst. Sci. Discuss.*, *16*, 4009–4022.

Mboh, C., J. Huisman, and H. Vereecken (2011), Feasibility of sequential and coupled inversion of time domain reflectometry data to infer soil hydraulic parameters under falling head infiltration, *Soil Sci. Soc. Am. J.*, *75*(3), 775–786.

Moysey, S. (2010), Hydrologic trajectories in transient Ground-Penetrating Radar reflection data, *Geophysics*, *75*(4), WA211–WA219.

Mualem, Y. (1976), A new model for predicting the hydraulic conductivity of unsaturated porous media, *Water Resour. Res.*, *12*(3), 513–522.

Muntz, A., L. Faure, and E. Laine (1905), Études sur la perméabilité des terres, faites en vue de l'arrosage, *Ann. Dir. Hydraul.*, *f33*, 45–53.

Nelder, J., and R. Mead (1965), A Simplex method for function minimization, *Comput. J.*, *7*, 308–313.

Perroux, K., and I. White (1988), Designs for disc permeameters, *Soil Sci. Soc. Am. J.*, *52*(5), 1205–1215.

Press, W., B. Flannery, S. Teukolsky, and W. Vettering (1988), *Numerical Recipes in C*, Cambridge Univ. Press, Cambridge, U. K.

Reynolds, W., and D. Elrick (1991), Determination of hydraulic conductivity using a tension infiltrometer, *Soil Sci. Soc. Am. J.*, *55*(3), 633–639.

Richards, L. (1931), Capillary conduction of liquids through porous mediums, *Physics N. Y.*, *1*(5), 318–333.

Roth, K., R. Schulin, H. Flühler, and W. Attinger (1990), Calibration of time domain reflectometry for water content measurement using a composite dielectric approach, *Water Resour. Res.*, *26*(10), 2267–2273.

Russo, D., and M. Bouton (1992), Statistical analysis of spatial variability in unsaturated flow parameters, *Water Resour. Res.*, *28*(7), 1911–1925.

Saintenoy, A., and J. Hopmans (2011), Ground penetrating radar: Water table detection sensitivity to soil water retention properties, *IEEE J. Selec. Top. Appl. Earth Obs. Remote Sens.*, *4*(4), 748–753.

Saintenoy, A., S. Schneider, and P. Tucholka (2008), Evaluating Ground-Penetrating Radar use for water infiltration monitoring, *Vadose Zone J.*, *7*(1), 208–214.

Sethian, J., and A. Popovici (1999), 3-D travel time computation using the fast marching method, *Geophysics*, *64*(2), 516–523.

Sheets, K. R., and J. M. Hendrickx (1995), Non invasive soil water content measurement using electromagnetic induction, *Water Resour. Res.*, *31*(10), 2401–2409.

Simunek, J., and M. T. van Genuchten (1996), Estimating unsaturated soil hydraulic properties from tension disc infiltrometer data by numerical inversion, *Water Resour. Res.*, *9*(32), 2683–2696.

Simunek, J., T. Vogel, and M. T. van Genuchten (1994), The SWMS-2D code for simulating water flow and solute transport in two-dimensional variably saturated media, *Res. Rep. 132*, USDA-ARS U.S. Salinity Lab., Riverside, Calif.

Simunek, J., M. T. van Genuchten, and M. Sejna (2008), Development and applications of the HYDRUS and STANMOD software packages, and related codes, *Vadose Zone J.*, *7*(2), 587–600.

Torczon, V. (1989), Multi-directional search: A direct search algorithm for parallel machines, PhD thesis, Rice Univ., Houston, Tex.

van Genuchten, M. T. (1980), A closed-form equation for predicting the hydraulic conductivity of unsaturated soils, *Soil Sci. Soc. Am. J.*, *44*(5), 892–898.

Vereecken, H., J. Huisman, H. Bogena, and J. Vanderborght (2008), On the value of soil moisture measurements in vadose zone hydrology: A review, *Water Resour. Res.*, *44*, W00D06, doi:10.1029/2008WR006829.

Vrugt, J. A., H. V. Gupta, W. Bouten, and S. Sorooshian (2003), A Shuffled Complex Evolution Metropolis algorithm optimization and uncertainty assessment of hydrologic models parameters, *Water Resour. Res.*, *39*(8), 1201, doi:10.1029/2002WR001642.

Vrugt, J. A., P. H. Stauffer, T. Wöhling, B. A. Robinson, and V. V. Vesselinov (2008), Inverse modeling of subsurface flow and transport properties: A review with new developments, *Vadose Zone J.*, *7*(2), 843–864.

Wright, M. (1996), Direct search methods: Once scorned, now respectable, in *Proceedings of the 1995 Dundee Biennial Conference in Numerical Analysis*, edited by D. Griffiths and G. Watson, pp. 191–208, Addison-Wesley, Harlow, U. K.

Zhou, Q., J. Shimada, and A. Sato (2001), Three-dimensional spatial and temporal monitoring of soil water content using electrical resistivity tomography, *Water Resour. Res.*, *37*(2), 273–285.